

X-RAYS FROM SUPERBUBBLES IN THE LARGE MAGELLANIC CLOUD. V. THE H II COMPLEX N11

MORDECAI-MARK MAC LOW

Max-Planck-Institut für Astronomie, Königstuhl 17, D-69117 Heidelberg, Germany; mordecai@mpia-hd.mpg.de

THOMAS H. CHANG, YOU-HUA CHU, AND SEAN D. POINTS

Department of Astronomy, University of Illinois, 1002 W. Green Street, Urbana, IL 61801;
 thomas@juno.as.utexas.edu, chu@astro.uiuc.edu, points@astro.uiuc.edu

R. CHRIS SMITH

Department of Astronomy, University of Michigan, 934 Dennison Building, Ann Arbor, MI 48109; chris@astro.lsa.umich.edu

AND

BART P. WAKKER

Department of Astronomy, University of Wisconsin, 475 N. Charter Street, Madison, WI 53706; wakker@astro.wisc.edu

Received 1997 April 1; accepted 1997 August 11

ABSTRACT

The giant H II complex N11 in the Large Magellanic Cloud contains OB associations at several different stages in their life histories. We have obtained *ROSAT* PSPC and HRI X-ray observations, Curtis Schmidt CCD images, echelle spectra in H α and [N II] lines, and *IUE* interstellar absorption line observations of this region. The central bubble of N11 has an X-ray luminosity a factor of only 3–7 brighter than that predicted for an energy-conserving superbubble, making this the first detection of X-ray emission from a superbubble without a strong X-ray excess. The region N11B contains an extremely young OB association analogous to the central association of the Carina Nebula, apparently still embedded in its natal molecular cloud. We find that N11B emits diffuse X-ray emission, probably powered by stellar winds. Finally, we compare the tight cluster HD 32228 in N11 to R136 in 30 Dor. The latter is a strong X-ray source, while the former is not detected, showing that strong X-ray emission from compact objects is not a universal property of such tight clusters.

Subject headings: ISM: bubbles — ISM: individual (N11) — Magellanic Clouds — X-rays: ISM

1. INTRODUCTION

Giant H II regions contain numerous massive stars. In these regions we expect that supernova remnants (SNRs) and stellar winds from the most massive stars will interact with interstellar gas to produce shocked, hot plasma that emits X-rays. Indeed, bright diffuse X-ray emission has been detected in two nearby giant H II regions: at levels of a few $\times 10^{35}$ ergs s $^{-1}$ in the Carina Nebula (Seward & Chlebowski 1982; Corcoran et al. 1994) and $\sim 10^{37}$ ergs s $^{-1}$ in the 30 Doradus Nebula (Chu & Mac Low 1990, hereafter Paper I; Wang & Helfand 1991a). Unfortunately, these giant H II regions are so complex that it is difficult to understand their observed X-ray properties.

It has been suggested that stellar winds alone power the X-ray-emitting plasma in the Carina Nebula, since no classical SNR signatures exist, and since the diffuse X-ray morphology roughly follows the distribution of early-type stars (Seward & Chlebowski 1982; Walborn & Hesser 1982). However, interstellar absorption observations show the presence of high-velocity gas at $\Delta V = \pm 200$ –300 km s $^{-1}$ (Walborn 1982; Walborn & Hesser 1982), and such large velocity offsets have otherwise only been seen in SNRs (Jenkins, Silk, & Wallerstein 1976; Fitzpatrick & Savage 1983). Could there be hidden SNRs producing both X-ray emission and high-velocity gas in the Carina Nebula?

The diffuse X-ray emission in 30 Dor correlates well with its large shell structures, reminiscent of the isolated X-ray bright superbubbles described by Paper I and by Wang & Helfand (1991b). In these X-ray bright superbubbles, the observed X-ray luminosities exceed by as much as an order

of magnitude the luminosities predicted by pressure-driven bubble models (Weaver et al. 1977; Paper I). The source of the X-ray emission has been proposed to be SNRs hitting the shell walls (Paper I; Wang & Helfand 1991b) or mass-loaded SNRs within the bubble (Arthur & Henney 1996). We have also identified superbubbles that are faint in X-rays and found that the upper limits on their X-ray luminosities are consistent with those expected in pressure-driven bubble models (Chu et al. 1995, hereafter Paper III). Can we convincingly detect X-ray emission from superbubbles at levels predicted by pressure-driven bubble models?

An *Einstein* High Resolution Imager (HRI) observation of the core of 30 Dor showed two pointlike sources, each having an X-ray luminosity of nearly 10^{36} ergs s $^{-1}$ (Wang & Helfand 1991a). These two sources are projected near two tight clusters of massive stars, R136 and R140 (N. R. Walborn & F. Seward, private communication 1989); however, the luminosities exceed those of stellar emission by at least 2–3 orders of magnitude. Using recent *ROSAT* HRI observations, Wang (1995) identified Mrk 34 (10" from R136) and R140 as their optical counterparts and concluded that these X-ray sources are Wolf-Rayet + black hole binaries. Do such sources always occur in similar tight clusters of massive stars?

To help answer these questions, we have studied the LMC H II complex N11, the second-ranking H II complex in the LMC (Kennicutt & Hodge 1986). N11 (Henize 1956) contains four OB associations: LH 9, LH 10, LH 13, and LH 14 (Lucke & Hodge 1970). LH 9 is surrounded by a

large superbubble, while LH 10, LH 13, and LH 14 are embedded in bright, compact H II regions along the periphery of the superbubble, designated as the B, C, and E components of N11, respectively (see Fig. 1).

We have selected N11 for three reasons. First, the OB association LH 10 within N11B contains several O3 stars similar to those in the OB associations in the Carina Nebula, but the surrounding H II region N11B has no high-velocity gas indicative of possible hidden SNRs. If the X-ray emission in the Carina Nebula comes only from hidden SNRs, we would expect N11B to have a much lower X-ray luminosity. Second, the large superbubble surrounding LH 9 in N11 forms a good candidate to observe directly X-ray emission from a pressure-driven bubble. Third, the tight core of the association LH 9, HD 32228, contains at least 16 early-type stars with the principal components being WC5-6 and O9.5 II (Parker et al. 1992), analogous to R136 or R140 in 30 Dor, and so can be examined for pointlike X-ray sources.

N11 has recently been observed by Rosado et al. (1996) using an imaging Fabry-Perot interferometer to map the velocity structure in H α and [O III] lines. Echelle spectroscopy in H α along a north-south (N-S) line cutting through the main shell of N11 was performed by Meaburn et al. (1989). Parker et al. (1992, 1996) studied the stellar content of the central associations of the main shell (LH 9), and of N11B (LH 10), and Walborn & Parker (1992) compared N11B with 30 Dor. Maps of CO tracing molecular gas in the region have been presented by Cohen et al. (1988), Israel & de Graauw (1991), Caldwell (1996), and Caldwell & Kutner (1996).

In the next section, we describe observations of N11 in the visible, ultraviolet, and X-ray wavelengths that we have obtained in order to better answer the questions raised above and understand the dynamics of this region. In § 3 we define the X-ray source regions and describe the analysis of the X-ray data. In § 4 we derive the X-ray luminosity predicted by the pressure-driven bubble model. In § 5 we

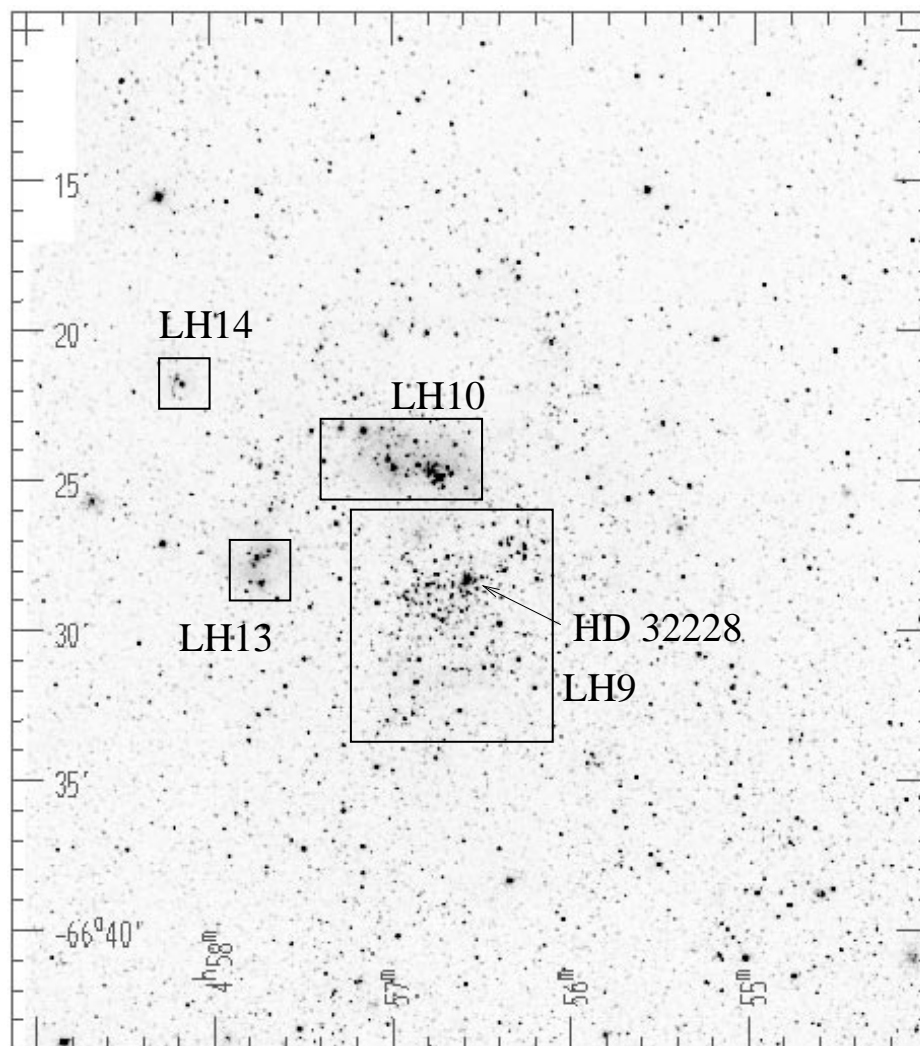


FIG. 1a

FIG. 1.—(a) Green continuum image of N11 from the Curtis Schmidt, showing the distribution of stars. The OB associations and HD 32228 are marked. (b) H α Schmidt image of N11 to show the distribution of ionized gas. The OB association LH 9 lies in the center of the main shell; LH 10, LH 13, and LH 14 lie in N11B, N11C, and N11E, respectively. The compact cluster HD 32228 lies just east of the center of the main shell, at R.A. 04^h56^m34^s.5, decl. $-66^{\circ}28'25''$ (J2000). The three echelle slit positions are marked.

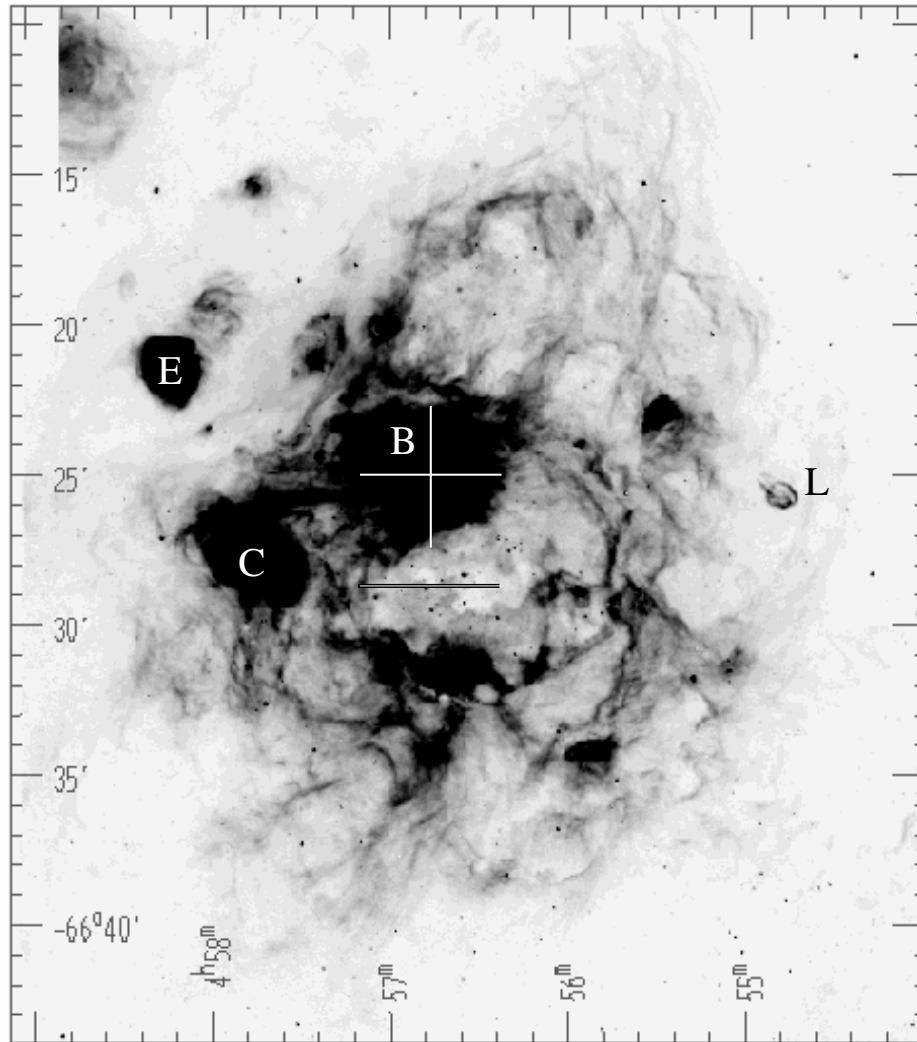


FIG. 1b

attempt to interpret the observations of the various parts of the N11 complex, and finally in § 6 we summarize our conclusions.

2. OBSERVATIONS

We have observed N11 using a number of different techniques. The distribution of the denser, photoionized gas in shell walls and molecular cloud surfaces can be seen in optical emission line images that we obtained using a CCD camera on the Curtis Schmidt telescope at the Cerro Tololo Inter-American Observatory (CTIO). In order to trace the hot gas produced by shocks in stellar wind bubbles or SNRs, we used pointed X-ray observations with the *ROSAT* Position Sensitive Proportional Counter (PSPC) and High Resolution Imager (HRI). The kinematics of the photoionized gas are revealed by high-dispersion, long-slit spectra obtained with an echelle spectrograph on the CTIO 4 m telescope, and high-dispersion UV spectra obtained with the *International Ultraviolet Explorer* (IUE). In this section, we describe these observations.

2.1. Curtis Schmidt CCD Images

Multiple optical CCD images of two fields of the N11 complex were obtained with the Curtis Schmidt telescope at

CTIO on 1995 January 28. A front-illuminated Thomson 1024 × 1024 CCD was used; its 19 μm pixel size corresponded to 1''.835 pixel⁻¹. The field of view was 31''.3. Narrowband filters of Hα ($\lambda_c = 6564 \text{ Å}$, $\Delta\lambda = 20 \text{ Å}$), [S II] ($\lambda_c = 6724 \text{ Å}$, $\Delta\lambda = 50 \text{ Å}$), and [O III] ($\lambda_c = 5010 \text{ Å}$, $\Delta\lambda = 50 \text{ Å}$) were used to isolate diagnostic emission lines. Broader red and green filters ($\lambda_c = 6840 \text{ Å}$, $\Delta\lambda = 95 \text{ Å}$ and $\lambda_c = 5133 \text{ Å}$, $\Delta\lambda = 92 \text{ Å}$, respectively) were used to obtain emission-line-free continuum images, which provide templates for continuum subtraction from the emission-line images. The data were reduced using the IRAF¹ software package for bias subtraction, flat-fielding, and sky subtraction. The images of the two fields were mosaicked after multiple frames in each field were shifted and combined. The total exposure times for each position in the final mosaicked images are 2700 s in Hα, 4800 s in [S II], 3600 s in [O III], 1800 s in the red continuum and 1500 s in the green continuum. Figure 1a presents the green continuum image to show the location of stars, and Figure 1b presents the continuum-subtracted Hα image to show the distribution of ionized gas.

The flux calibration of the CCD images was made using observations of photometric standard stars. The sky-

¹ IRAF is distributed by the National Optical Astronomy Observatories (NOAO).

subtracted H α fluxes of N11 determined from the CCD images agree within 10% uncertainty with those determined from the photoelectrically calibrated PDS scans of Kennicutt & Hodge's (1986) photographic plates, kindly provided to us by Dr. R. C. Kennicutt. The H α fluxes are converted to emission measures, assuming an electron temperature of 10^4 K. The faintest nebulosities detected by the deep CCD images have emission measures of ~ 10 cm $^{-6}$ pc; the brightest parts have emission measures over 10^5 cm $^{-6}$ pc.

2.2. ROSAT X-Ray Observations

We used the *ROSAT* PSPC and HRI to obtain X-ray observations of N11. The PSPC is sensitive to the energy range of 0.1–2.4 keV, while the HRI is sensitive to 0.1–2.0 keV. The PSPC has an energy resolution of $\sim 45\%$ and an on-axis angular resolution of $\sim 30''$ at 1 keV. The HRI has a very poor energy resolution but a higher angular resolution: $\sim 5''$. Detailed information about the performance and characteristics of these instruments can be found in Pfeiffermann et al. (1986) or the *ROSAT* Mission Description (1991).

The PSPC observation of N11 was numbered rp900320. A total integration time of 29.65 ks was obtained, with 16.7

ks between 1992 November 16 and 1992 December 4 and 12.9 ks during 1993 February 14–15. The PSPC was operated in the low-gain state throughout the observation. The HRI observation of N11 was numbered rh900321. A total integration time of 27.1 ks was obtained between 1992 October 25 and 1993 February 18.

The PSPC observation is best suited for revealing diffuse X-ray emission. To maximize the signal-to-noise (S/N) ratio without significantly degrading the spatial resolution, we have binned the PSPC image, which is heavily oversampled compared with its instrumental resolution, by a factor of 10 to obtain a pixel size of $5''$ pixel $^{-1}$, and smoothed the image with a Gaussian of $\sigma = 5$ pixels, or $25''$. The smoothed PSPC image in the 0.1–2.4 keV band is shown in Figure 2. To show the relationship between H α and X-ray emission, Figure 3 presents an H α image overlaid by X-ray contours derived by binning the PSPC image by a factor of 8 and smoothing it with a Gaussian of $\sigma = 2$ pixels, or $8''$.

The HRI observation is better suited for revealing point sources. For a $6''$ diameter detection cell, no point sources are detected in N11 and its vicinity at $\geq 3\sigma$ levels, or 2.3×10^{-4} counts s $^{-1}$. This count rate corresponds to a luminosity of 4×10^{33} ergs s $^{-1}$ (at a distance of 50 kpc for the LMC as given by Panagia et al. 1991), using the conver-

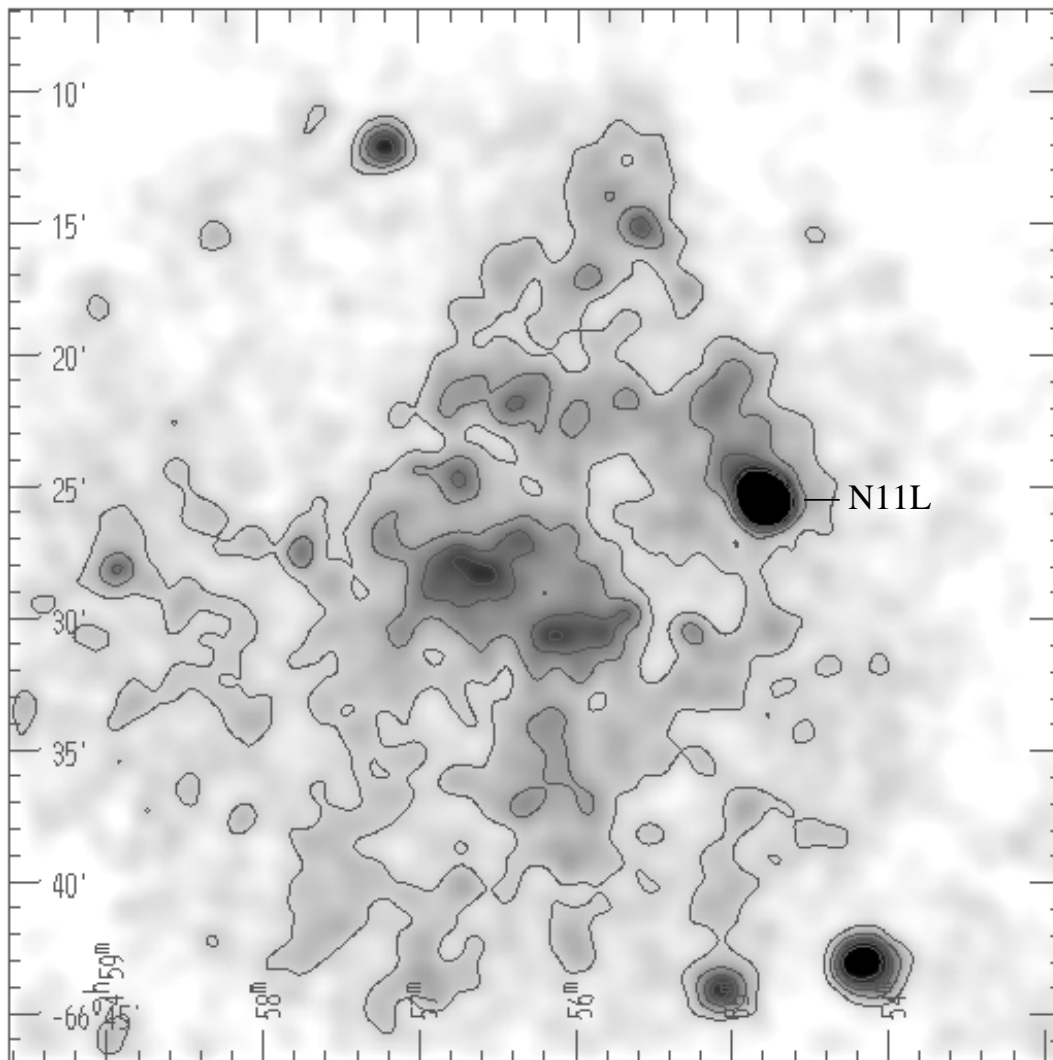


FIG. 2.—X-ray image of the N11 region. The PSPC image was binned by a factor of 10 and smoothed with a Gaussian of $\sigma = 25''$. The R.A. and decl. are in J2000. The contours are at 10%, 15%, 20%, 25%, and 30% of the peak brightness of the supernova remnant N11L at $04^{\text{h}}54^{\text{m}}48^{\text{s}}.5$, $-66^{\circ}25'45''$.

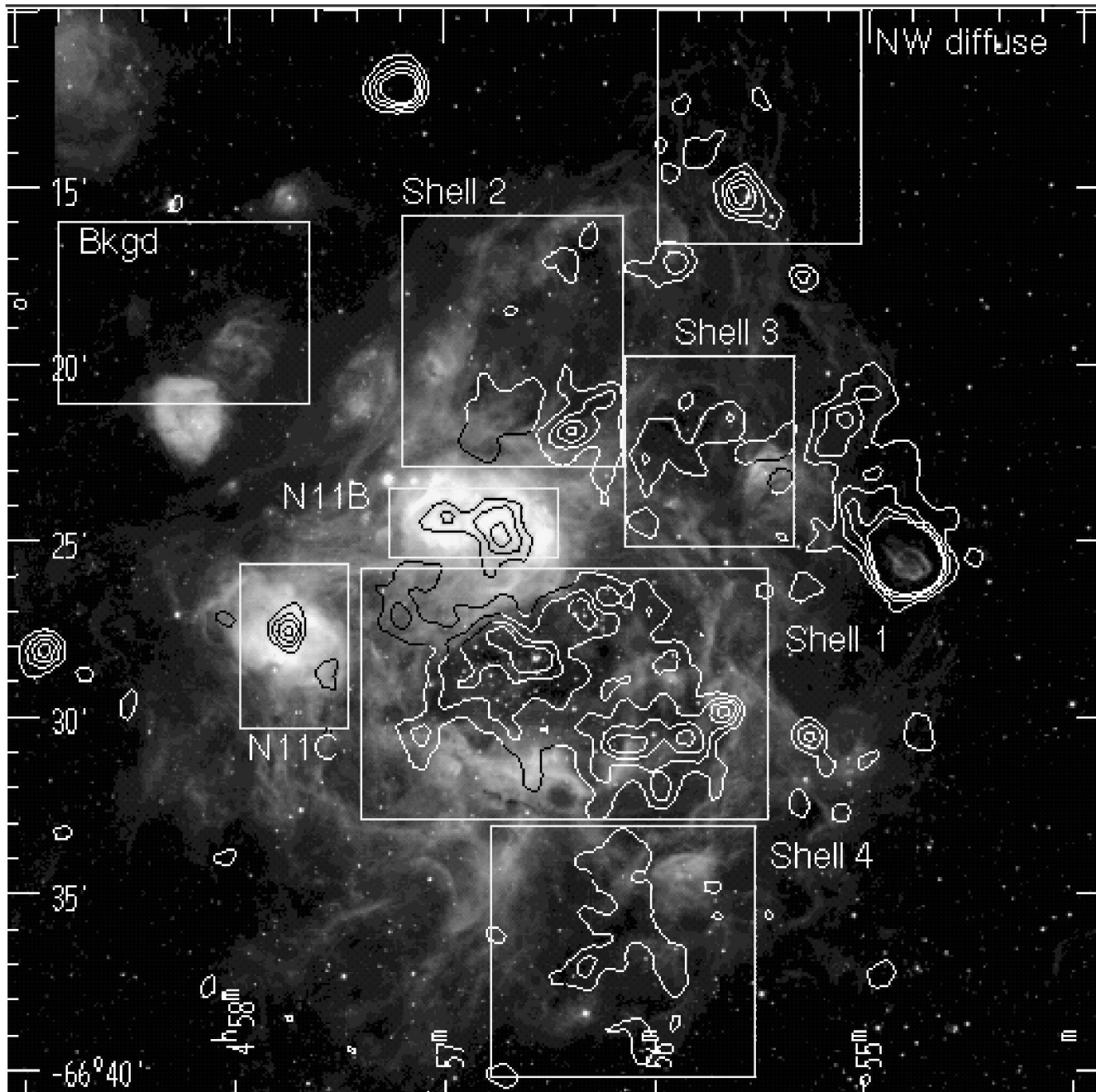


FIG. 3.—Contours of X-ray emission superimposed on our Curtis Schmidt H α image. This X-ray image was derived by binning the PSPC image by a factor of 8 and smoothed by a Gaussian of $\sigma = 8''$. The contours are 10%, 13%, 16%, and 20% of the peak brightness of the supernova remnant N11L at $04^{\text{h}}54^{\text{m}}48^{\text{s}}.5$, $-66^{\circ}25'45''$. The R.A. and decl. are in J2000. The source and background regions are marked.

sion factor for a 5×10^6 K plasma and an absorption column density of $\log N_{\text{H}} = 21.5$ in Figure 10.3 of the *ROSAT* Mission Description (1991).

The SNR N11L (the bright source on the western edge of N11) is the only obvious X-ray source in the HRI image. We have binned the HRI image by a factor of 10, resulting in a pixel size of $5'' \text{ pixel}^{-1}$, and smoothed it with Gaussians of $\sigma = 50''$ – $100''$. Regions with bright diffuse X-ray emission detected by the PSPC are also detected in the heavily smoothed HRI images. Since these heavily smoothed HRI images have effective resolutions comparable to or lower than the PSPC's resolution, and since the smoothed HRI image has lower S/N ratios than the PSPC image, the HRI

image is not shown in this paper. Analysis of the HRI image of N11L will be reported in another paper.

2.3. Long-Slit Echelle Spectroscopy of Emission Lines

We obtained high-dispersion spectra of N11 using the echelle spectrograph with the long-focus red camera on the 4 m telescope at CTIO on 1995 January 28. A 79 lines mm^{-1} echelle grating was used. We used the instrument as a single-order, long-slit spectrograph by inserting a postslit interference filter and replacing the cross-dispersing grating with a flat mirror, so that a single echelle order around H α and [N II] $\lambda\lambda 6548, 6583$ could be imaged over the entire slit. The data were recorded with a Tek 2048 \times 2048 CCD using

Arcon 3.6 controller. The pixel size was $24 \mu\text{m pixel}^{-1}$, which provided a sampling of 0.082 \AA (3.75 km s^{-1}) along the dispersion and $0''.267$ on the sky. Spectral coverage was effectively limited by the bandwidth of the interference filter to 125 \AA . Coverage along the slit was $245''$; however, the outermost $20''$ at each end of the slit is seriously affected by vignetting. The instrumental profile, as measured from Th-Ar calibration lamp lines, was $16.1 \pm 0.8 \text{ km s}^{-1}$ FWHM at the $\text{H}\alpha$ line. This range includes variations in the mean focus and variations in the focus over a single spectrum. Spatial resolution was determined by the seeing, which was $\sim 1''$. The exposure times were 10–20 minutes.

The data were bias subtracted at the telescope and later processed using the IRAF software for flat-fielding, wavelength calibration, distortion correction, and removal of cosmic rays. Wavelength calibration and distortion correction were performed using Th-Ar lamp exposures taken in the beginning of each night. To eliminate velocity errors due to flexures in the spectrograph, the absolute wavelength scale in each spectrum was referenced to the geocoronal $\text{H}\alpha$ line at zero observed velocity.

Three slit positions were observed in N11. One east-west (E-W) oriented slit was centered on the star Sk $-66^\circ 31'$ (R.A. $04^{\text{h}}56^{\text{m}}40^{\text{s}}$, decl. $-66^\circ 33'33''$, J2000) near the center of the main shell in N11. The other two slit positions were centered on the star PGMW 3021 (Parker et al. 1992) in N11B $\sim 244''$ north of Sk $-66^\circ 31'$, with one slit E-W orient-

ed and the other N-S oriented. The slit positions are marked in Figure 1b, and the echellograms are presented in Figure 4. The spectral features detected in the echellograms (Fig. 4) include the $\text{H}\alpha$ line and the $[\text{N II}] \lambda\lambda 6548, 6583$ lines, in addition to the faint telluric airglow features of OH. The $[\text{N II}]$ lines are too weak to be of much use.

2.4. High-Dispersion IUE Observations

High-dispersion IUE spectra are available for two stars in N11: SWP 15065 for HD 32228 (Sk $-68^\circ 28'$) and SWP 49304 for Sk $-66^\circ 31'$. The spectrum of HD 32228, retrieved from the IUE archives and presented by Chu et al. (1994), shows C IV and possibly Si IV interstellar absorption at $\sim 270 \text{ km s}^{-1}$ and S II and Si II at $\sim 290 \text{ km s}^{-1}$. The spectrum of Sk $-66^\circ 31'$, an O9 I star, was obtained by us in the sixteenth episode of IUE. Unfortunately, this spectrum is too noisy to be very useful, although by much smoothing one can find features that could be Magellanic C IV and possibly Si IV absorption.

3. ANALYSIS OF X-RAY DATA

We have used the software package PROS to analyze the PSPC X-ray data. We first define source and background regions (detailed in § 3.1), then extract the background-subtracted, vignetting-corrected count rate and spectral energy distribution for each source region. The observed spectral energy distribution is a convolution of the intrinsic

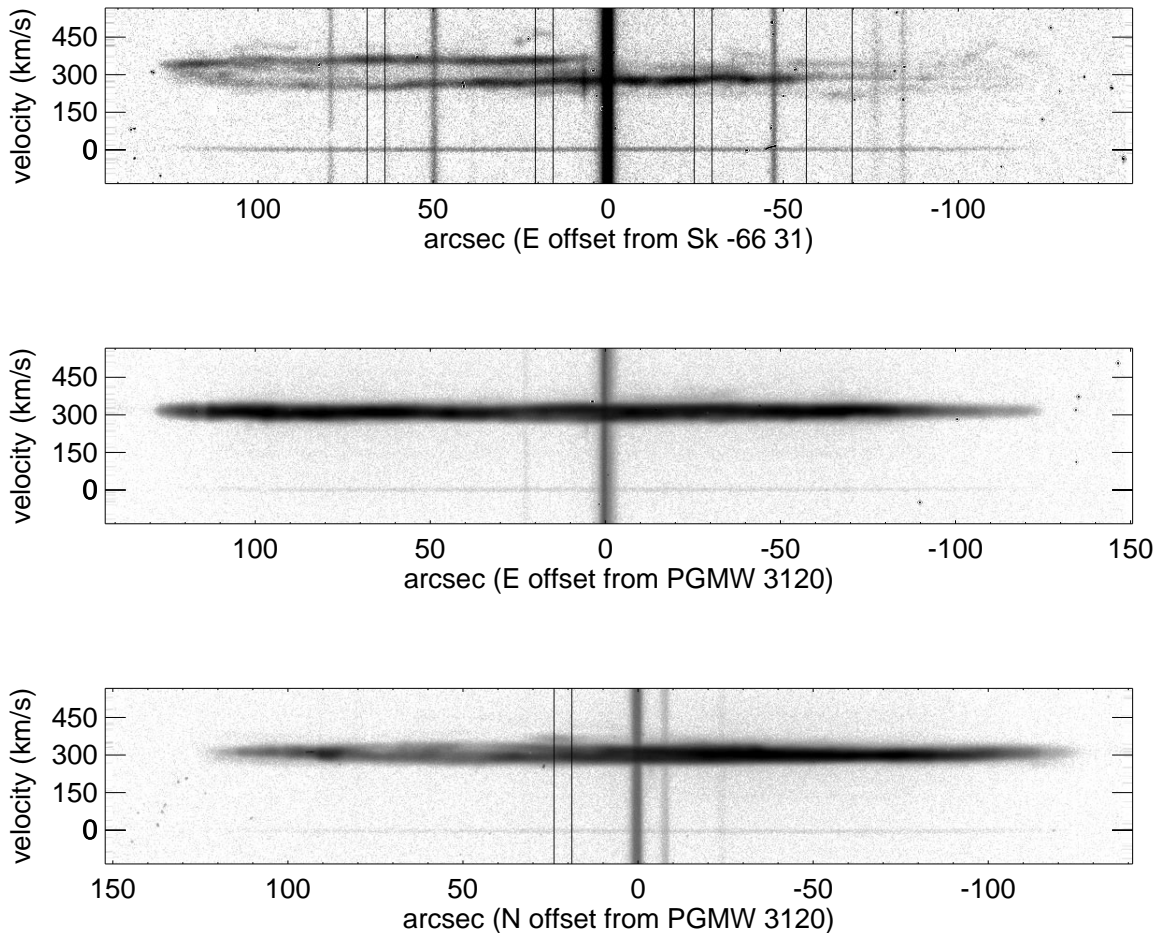


FIG. 4.—Echellograms of N11. (a) E-W oriented slit centered on Sk $-66^\circ 31'$ close to the center of the main shell. (b) E-W oriented slit $244''$ N, in N11B, centered on the star PGMW 3021. (c) N-S oriented slit also crossing the star PGMW 3021 in N11B. The profiles shown in Figs. 7 and 8 are drawn from the regions bounded by the thin black lines. Unvignetted slit lengths are $3'.5$.

spectrum, foreground absorption, and the instrumental response. The instrumental response of the *ROSAT* PSPC is well calibrated. It is possible to fold the instrumental response into plasma emission models (e.g., Raymond & Smith 1977) and fit the results to the observed spectral energy distribution in order to determine the plasma temperature kT , foreground absorption N_H , and X-ray luminosity L_x . We can express the foreground absorption in terms of hydrogen column density N_H by using the effective cross sections per hydrogen atom of Morrison & McCammon (1983). The goodness of our spectral fits is shown by χ^2 grid plots in the kT - N_H plane. Using a 30% cosmic (solar)

abundance that is appropriate for the LMC, we have made spectral fits to the observed spectral energy distribution (Fig. 5) and generated χ^2 grid plots (Fig. 6). The best-fit kT , $\log N_H$, and L_x are listed in the top section of Table 1.

The number of counts received from our sources is usually too low to constrain the spectral fits well. Therefore, we use other independent estimates of foreground absorption to confine the plasma temperature fits. The various methods we use to estimate absorption columns are described in detail below in § 3.2. The plasma temperature kT and the absorption column N_H are then used to determine the intrinsic X-ray fluxes and luminosities. The best

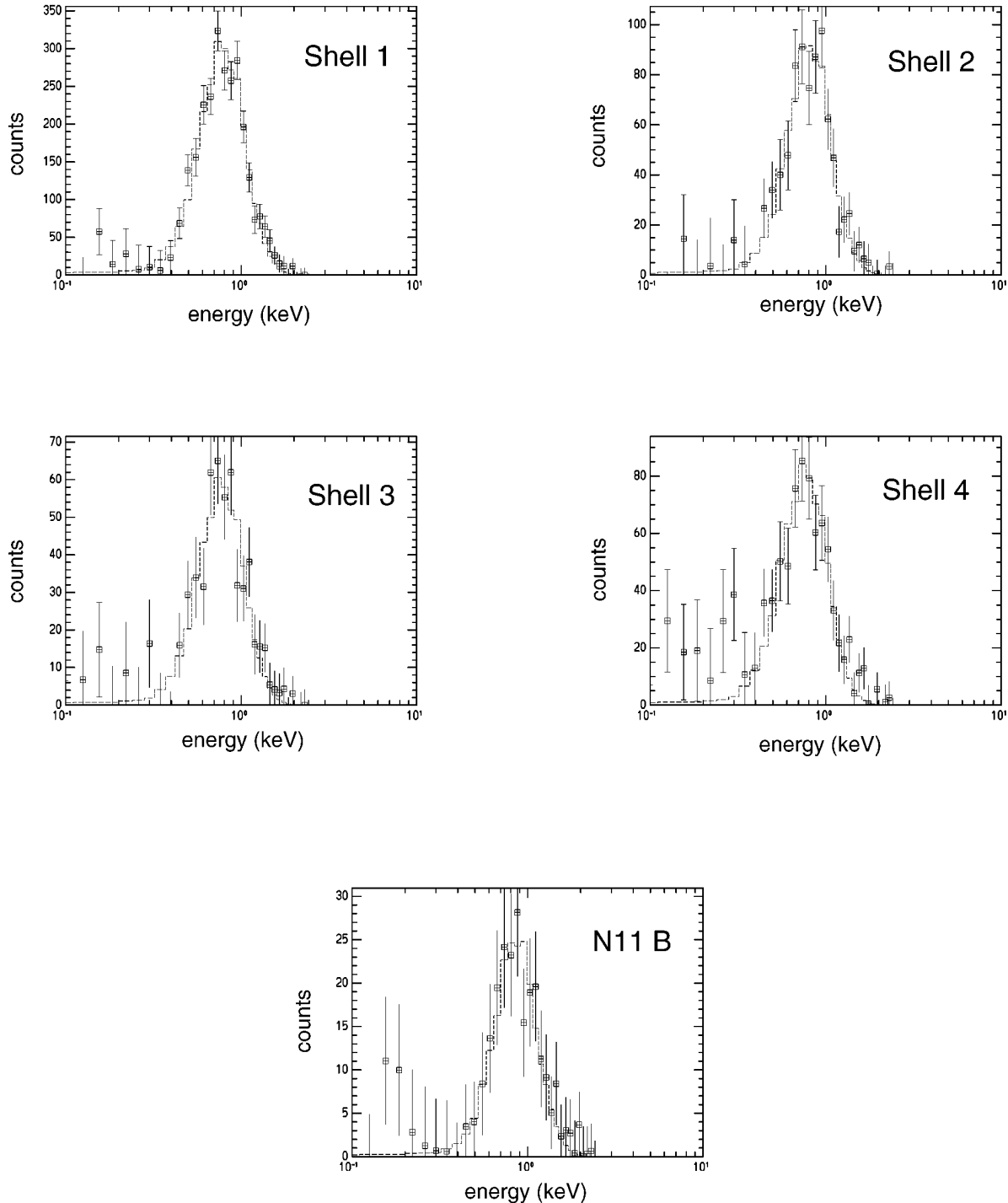


FIG. 5.—Observed spectral energy distributions and the best model fits *without* constraints on N_H

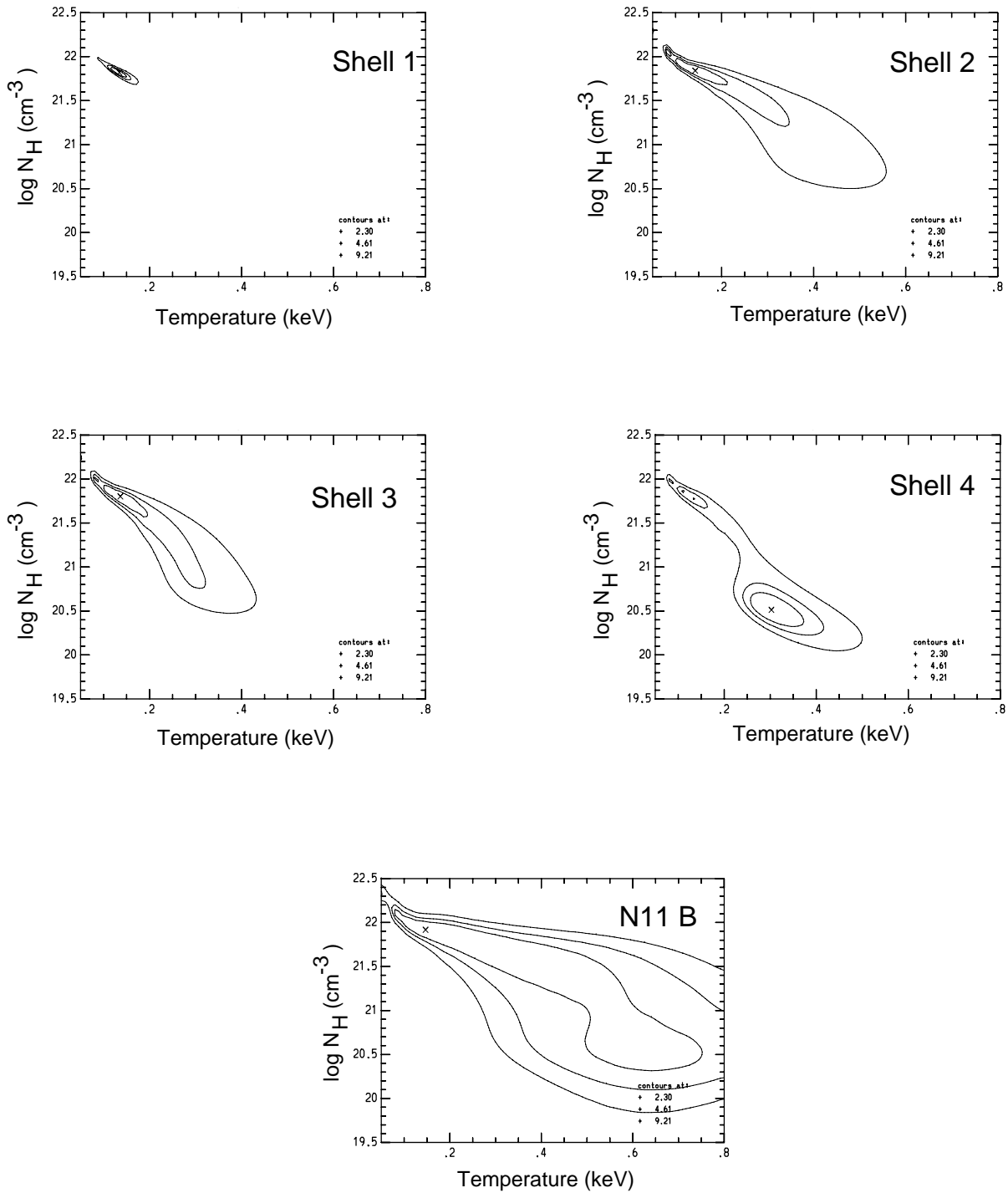


FIG. 6.— χ^2 grid plots for the spectral fits shown in Fig. 5. The three contours correspond to 68%, 90%, and 99% confidence levels. Temperatures are given in keV.

independently estimated $\log N_{\text{H}}$, the corresponding best-fit kT , and the resultant L_x are listed in the bottom section of Table 1.

When absorbing column densities are of order 10^{22} cm^{-2} or higher, emission below about 0.5 keV is almost completely absorbed, even though *ROSAT* is sensitive down to 0.1 keV. The intrinsic luminosity in the 0.1–2.4 keV band is then dominated by the absorption correction in the 0.1–0.5 keV range, but virtually no photons are detected in this range, giving very uncertain results. We do give the luminosities derived for both 0.1–2.4 keV and 0.5–2.4 keV bands

in Table 1. Although we used the 0.1–2.4 keV band to find conservative upper limits for X-ray dim superbubbles in Paper III, the high luminosities given in Table 1 from considering this full band in regions with high absorption appear unphysical. The luminosities derived from the 0.5–2.4 keV band are more physically meaningful.

3.1. Selection of Source and Background Regions

There is excellent correspondence between the X-ray emission and interstellar structures revealed in the $\text{H}\alpha$ image. Frequently, enhanced X-ray emission is seen within

TABLE 1
OBSERVED X-RAY PROPERTIES OF N11

Region	Shell 1	Shell 2	NW Diffuse	Shell 3	Shell 4	N11B
Free N_H Fits ^a						
kT (keV)	0.2–0.1	0.5–0.1	0.6–0.1	0.4–0.1	0.5–0.1	1.0–0.1
$\log N_H$	21.6–22.0	20.5–22.0	20.0–22.0	20.5–22.0	20.1–22.0	20.0–22.0
$\log L_x$ (0.1–2.4) ^b	36.73–39.37	35.03–38.87	34.64–38.54	34.87–38.66	34.93–38.81	34.43–38.29
$\log L_x$ (0.5–2.4) ^b	36.32–38.12	34.87–37.62	34.48–37.29	34.69–37.41	34.78–37.56	34.23–37.05
Fixed N_H Fits						
kT (keV)	0.32–0.29	0.38–0.36	0.32–0.30	0.29–0.28	0.27–0.25	0.47–0.34
$\log N_H$	20.9–21.1	20.9–21.1	20.9–21.1	20.9–21.1	20.9–21.1	21.3–21.6
$\log L_x$ (0.1–2.4) ^b	35.75–35.87	35.17–35.27	34.92–35.04	35.08–35.21	35.28–35.40	34.74–35.17
$\log L_x$ (0.5–2.4) ^b	35.52–35.62	34.98–35.07	34.69–34.79	34.83–34.94	35.00–35.10	34.58–34.95

^a Parameter ranges give 99% confidence levels.

^b In units of ergs s^{-1} , with the energy band given in keV.

large shells. Guided by the $H\alpha$ image, we divide the X-ray emission from N11 into seven source regions, as shown in Figure 3 and listed in Table 1. Four of these regions are associated with large shells. We define “shell 1” as the main shell of N11, encompassing LH 9. “Shell 2” is the faint shell structure 10' north of the main shell. “Shell 3” is the small shell structure northwest (NW) of Shell 1 and southwest (SW) of Shell 2. “Shell 4” is the shell located 10' south of the main shell. Two source regions are selected to include the B and C components of N11, respectively. We notice faint $H\alpha$ filaments correlated with diffuse X-ray emission extending NW of shell 2, suggesting a blowout into a lower density region, which we define as the “NW diffuse” source region. The X-ray data of these regions are analyzed individually.

The selection of background regions is important for the analysis of extended emission. A *ROSAT* PSPC mosaic of the LMC (Fig. 3 of Snowden & Petre 1994) shows that N11 appears as an emission wedge (colored in green and yellow) flanked by highly absorbed regions (deep blue, purple areas) on the east and west sides, while its south side is connected with a diffuse emission region (green areas) that extends over 1000 pc to the south. We have tested two background regions: the low background region to the east labeled on Figure 3, as well as another higher background region to the southwest of N11. It is not clear whether the extended emission observed to the south actually contributes to the emission from N11, so we have conservatively chosen the lower background for our quoted results. The higher background produces $\sim 30\%$ lower fluxes for shell 1 and N11B and will produce somewhat larger differences for fainter sources. Thus, our extracted X-ray fluxes and luminosities should be interpreted as upper limits. Because of the relatively large off-axis position of the background region, differential vignetting corrections for the source regions and the background region have been applied, after the charged particles are removed.

3.2. Independent Estimates of Absorption Columns

Soft X-rays are absorbed by all phases of the interstellar medium (ISM). We have used two methods to estimate the ranges of absorption column densities. As described below, both methods suffer from large uncertainties.

In the first method we limit the possible range in absorption column N_H by using previous observations of atomic and molecular gases and our current observations of ionized gas toward N11. An H I survey of the LMC by

Rohlfs et al. (1984) has shown a range of LMC H I column density of $(1.8\text{--}2.9) \times 10^{21} \text{ cm}^{-2}$ in the four pointings near N11, with a beam size of 15'. A Galactic foreground H I column density of $N_H = (5.6 \pm 2.0) \times 10^{20} \text{ cm}^{-2}$ was derived by Schwering & Israel (1991) using the large-scale H I survey by Cleary, Heiles, & Haslam (1979).

A high-resolution ESO/SEST survey shows a molecular cloud complex roughly encircling the N11 complex. Except for N11B, X-ray emission is not observed from any regions containing CO, possibly due to obscuration by the molecular clouds. The clouds show a peak CO intensity, $I_{\text{CO}} = 20 \text{ K km s}^{-1}$ (Israel et al. 1993). To translate this into a column density of H_2 , we scale the Galactic CO/ H_2 conversion ratio $X_{\text{MW}} = N_{\text{H}_2}/W_{\text{CO}} = 2.3 \times 10^{20} \text{ cm}^{-2} \text{ K}^{-1} \text{ km}^{-1} \text{ s}$ (Bloemen 1989) by the LMC metallicity of $\frac{1}{3}$. The observed CO intensity then corresponds to a N_{H_2} of $\sim 1 \times 10^{21} \text{ cm}^{-2}$.

Using our calibrated CCD $H\alpha$ images, we find emission measures of $4 \times 10^4 \text{ cm}^{-6} \text{ pc}$ in N11B and less than $1 \times 10^3 \text{ cm}^{-6} \text{ pc}$ in shells and other low surface brightness areas. Assuming the depth of the $H\alpha$ emission region is as large as the width of the emission region, we estimate ionized hydrogen column densities of $\sim 3.5 \times 10^{21} \text{ cm}^{-2}$ in N11B and $\sim 2 \times 10^{20} \text{ cm}^{-2}$ in shells and low surface brightness areas.

By combining these values we can estimate upper and lower limits to the absorbing hydrogen column density. For the lower limit, we assume that N11 is in front of all the LMC H I and that no more than half of the ionized gas in N11 contributes to the absorption column, so that the lower limit is the sum Galactic $N_{\text{HI}} + \frac{1}{2}\text{LMCN}_{\text{HII}}$. We use the appropriate H II column densities for the different regions as given above. For N11B this yields a lower limit of $\log N_H = 21.3$ and $\log N_H = 20.9$ for the other regions. For the upper limit, we examine the CO image of Caldwell (1996). In N11B, the only X-ray-emitting region that coincides with strong CO emission, we use the sum Galactic $N_{\text{HI}} + \frac{1}{2}(\text{LMCN}_{\text{HII}} + \text{LMCN}_{\text{HI}} + 2\text{LMCN}_{\text{H}_2})$ as an upper estimate, while in regions lacking CO emission we neglect the H_2 contribution entirely. This gives an upper limit of $\log N_H = 21.6$ for N11B and $\log N_H = 21.3$ for the other regions.

The second method to estimate absorption column uses optical extinction of stars embedded in the X-ray source regions. An overall average reddening of $E(B-V) = 0.05$ mag has been found in the stars of LH 9, the OB association in the main N11 shell, and $E(B-V) = 0.17$ mag in LH 10 in N11B (Parker et al. 1992). Brunet (1975) has reported an

average Galactic foreground reddening of $E(B-V) = 0.07$ mag. However, small-scale variations in Galactic reddening ranging from 0.0 to 0.15 mag toward the LMC have been found by Oestreicher et al. (1995) using a more complete sample of 1500 Galactic foreground stars. We adopt a Galactic gas-to-dust ratio of $N_H/E(B-V) = 4.8 \times 10^{21} \text{ cm}^{-2} \text{ mag}^{-1}$ (Bohlin et al. 1978) and an LMC gas-to-dust ratio of $2.4 \times 10^{22} \text{ cm}^{-2} \text{ mag}^{-1}$ (Fitzpatrick 1986). Adopting the reddening values of Parker et al. (1992), we estimate $20.3 \leq \log N_H \leq 21.1$ for the main shell and $21.1 \leq \log N_H \leq 21.6$ for N11B. By the same arguments, we can make an independent estimate of $20.9 \leq \log N_H \leq 21.6$ using the LMC intrinsic reddening map of Oestreicher & Schmidt-Kaler (1996).

These values agree well with our estimates from the emission-line observations of the ISM described above. We use a combination of the two estimates to constrain the absorption column densities, taking the lower of the two upper limits and the upper of the two lower limits to give the most likely range of N_H . The range of N_H that we have actually used for each region is listed in the bottom section of Table 1.

4. X-RAY EMISSION FROM PRESSURE-DRIVEN BUBBLE MODEL

To predict the X-ray luminosity from a pressure-driven bubble we follow the procedure described in Paper I, as corrected in Paper III. By assuming that conductive evaporation determines the interior structure of the bubble (Weaver et al. 1977), we can compute the X-ray luminosity if we know the radius of the bubble in parsecs, R_{pc} , its expansion velocity in km s^{-1} , v_5 , and the emission measure in $\text{H}\alpha$ on a tangential path through the shell in $\text{cm}^{-6} \text{ pc}$, EM . If we assume that the thickness of the shell $\Delta R \ll R$, the electron temperature $T_e \simeq 10^4$, and the mean atomic mass of the ambient medium $\mu_a = (14/11)m_H$, we can use equations (7)–(10) from Paper III to derive the X-ray luminosity directly from the three observables:

$$L_x \simeq (6.7 \times 10^{29} \text{ ergs s}^{-1}) \xi I E M^{5/7} R_{\text{pc}}^{12/7} v_5^{1/7}, \quad (1)$$

where ξ is the metallicity, which we take to be 0.3 in the LMC, and I is a slowly varying function of the interior temperature of the bubble, which we can take to have value $I \sim 2$. The external density into which the bubble is expanding is then

$$n_0 \simeq (22 \text{ cm}^{-3}) E M^{1/2} v_5^{-3/2} R_{\text{pc}}^{-1/2}, \quad (2)$$

the age of the bubble in Myr is

$$t_6 = 0.59 R_{\text{pc}} / v_5, \quad (3)$$

and the mechanical luminosity L_{mech} from stellar winds and SNRs driving the bubble is

$$L_{\text{mech}} \simeq (8 \times 10^{30} \text{ ergs s}^{-1}) E M^{1/2} v_5^{3/2} R_{\text{pc}}^{3/2}. \quad (4)$$

The kinetic energy K of the shell in a pressure driven bubble can be derived by noting that the thermal energy of the interior is $U = (5/11) L_{\text{mech}} t$ (Weaver et al. 1977) and that $K + U = 50/77 L_{\text{mech}} t$ (Mac Low & McCray 1988), so

$$K = (15/77) L_{\text{mech}} t = (2.9 \times 10^{43} \text{ ergs}) E M^{1/2} v_5^{1/2} R_{\text{pc}}^{5/2}. \quad (5)$$

Alternatively, the final result can be derived by taking $K = (1/2) M v_s^2$, where the mass of the shell $M = (4/3) \pi R^3 \mu_a n_0$.

5. INTERPRETATION

5.1. Shell 1

In Paper I we showed that some LMC superbubbles are X-ray bright, by which we mean that they have X-ray luminosities much higher than predicted by the pressure-driven bubble model, while in Paper III we placed upper limits on the X-ray luminosities from several other superbubbles that were close to the prediction of the model. Here we derive the X-ray luminosity of shell 1 and show that it is only slightly X-ray bright, with a luminosity a factor of 3–7 brighter than predicted by the pressure-driven bubble model.

X-ray emission from the central region of N11 lies within the optical shell seen in $\text{H}\alpha$. Performing spectral fits with unconstrained parameters in this region shows a 99% confidence range in absorption and plasma temperature of $\log N_H = 21.6\text{--}22.0$ and $kT = 0.2\text{--}0.1 \text{ keV}$ (see Table 1). This absorption column density is much larger than the best estimates we derived in § 3.2. This large absorption column density might be caused by an artifact of spectral fits in *ROSAT*'s very soft energy band. *ROSAT* PSPC spectra can often be equally well fitted by a cool plasma with a large absorption column or by a hotter plasma with a lower absorption column. Sometimes, a runaway spectral fit converges to an extremely high absorption column and a low plasma temperature. If we constrain the column density to the values suggested in § 3.2, we can derive an X-ray luminosity of $(3.3\text{--}4.2) \times 10^{35} \text{ ergs s}^{-1}$ in the 0.5–2.4 keV band, again assuming a distance of 50 kpc to the LMC (Panagia et al. 1991).

The velocity structure of the main shell is quite complex. Figure 4a shows an echellogram from an E-W slit across the central region, while Figure 7 shows velocity profiles at four different points on that slit. The broadest splitting seen is some 120 km s^{-1} (Fig. 7a), suggesting an expansion velocity as high as 60 km s^{-1} . Meaburn et al. (1989) observed the $\text{H}\alpha$ line with an echelle spectrograph along a N-S line passing through HD 32228, crossing our slit just west of center. They find as many as five velocity components in the central region, which they attribute to multiple expanding shells in a cellular structure. Rosado et al. (1996) performed Fabry-Perot observations of the entire N11 complex in both $\text{H}\alpha$ and $[\text{O III}]$. They also found multiple components but concluded that the main shell could best be described as undergoing a general radial expansion at 45 km s^{-1} , with lower density interior gas undergoing more rapid, cellular expansion.

We now can find the luminosity predicted by the pressure-driven bubble theory. The typical emission measures of filaments around the edge of the bubble are in the range $600\text{--}900 \text{ cm}^{-6} \text{ pc}$. We take the expansion velocity to lie in the range $45\text{--}60 \text{ km s}^{-1}$. To find the physical radius of the bubble, we again use the distance to the LMC of 50 kpc, implying that $1' = 14.5 \text{ pc}$. We then estimate the X-ray-emitting bubble to have a radius $R = 55\text{--}65 \text{ pc}$. A pressure-driven bubble with these parameter ranges is predicted by equation (1) to have an X-ray luminosity $L_x = (0.6\text{--}1.2) \times 10^{35} \text{ ergs s}^{-1}$. This is a factor of 3–7 lower than the X-ray luminosity derived from the observations using constrained column densities: the main shell of N11 is somewhat X-ray bright.

The excess X-ray emission is most likely produced by an intermittent source, since N11 represents an intermediate case between the bubbles we described in Paper III that

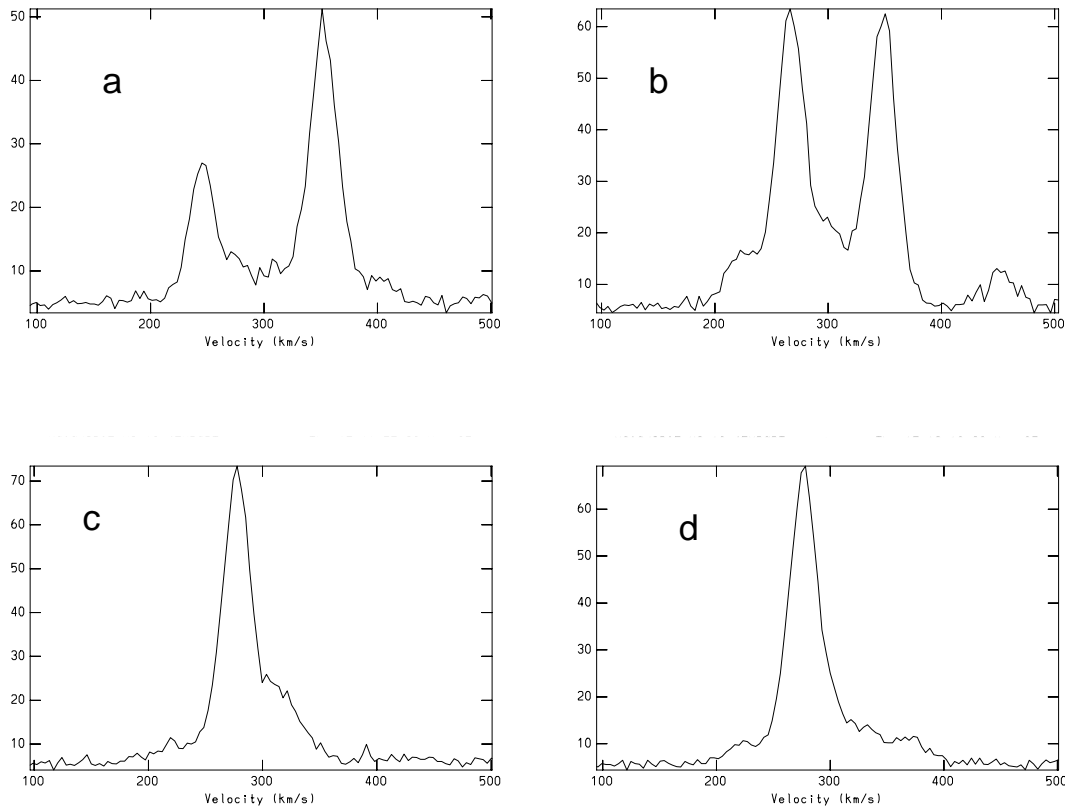


FIG. 7.—Velocity profiles at the four places designated by the thin black lines in Fig. 4a, moving from left to right

show no excess and those we described in Paper I with excesses of more than an order of magnitude. Arthur & Henney (1996) suggested that an SNR going off inside a bubble with embedded clumps could produce the excess. They ignored thermal evaporation of the clumps, suggesting that the evaporation could be suppressed by magnetic fields. Tao (1995) has shown, however, that fields cannot be tangled by dynamical means sufficiently to strongly suppress evaporation, so clumps would probably evaporate before being swept up by an SNR. Alternatively, we have suggested in Paper I that the excess X-ray emission is being produced as interior SNRs expanding in the low-density gas hit the ionized inner edge of the swept-up shell.

In Paper I we showed that X-ray emission expected from hidden SNRs hitting the shell should come from a broad region near the edge of or interior to the shell, depending on the angle of observation. X-ray emission from the hot interior should also be mildly edge brightened, as a result of the density increase toward the edge of a conductively evaporating bubble (Weaver et al. 1977). These predictions are consistent with the irregular but mildly edge-brightened X-ray morphology seen in Figure 2.

Using the same estimates of the observed parameters as above, we can examine the physical parameters of this bubble using equations (2)–(4). We find that the ambient density is $0.1\text{--}0.3\text{ cm}^{-3}$, a reasonable interstellar value. We note that there are clearly regions of far higher density in the ring around the main bubble, most noticeably traced by CO observations showing a ring of molecular clouds roughly coincident with the regions of highest H α intensity (Caldwell 1996; Israel & de Graauw 1991). However, these regions appear to have a low enough filling factor to not be dynamically important.

The mechanical luminosity driving the bubble (eq. [4]) lies in the range $L_{\text{mech}} = (3\text{--}6) \times 10^{37}\text{ ergs s}^{-1}$. Using only the 18 O-type stars in LH 9 that have been spectroscopically classified by Parker et al. (1992), and using the empirical mass loss rates and stellar wind terminal velocities appropriate for the spectral types (Conti & Underhill 1988), we derive an integrated wind mechanical luminosity of $3.3 \times 10^{37}\text{ ergs s}^{-1}$. It is conceivable that the WC5-6 star in HD 32228 and other unclassified early-type stars in LH 9 could supply the L_{mech} required to drive shell 1.

The total input energy $E = L_{\text{mech}}t$ in such a bubble is then $(0.6\text{--}1.2) \times 10^{51}\text{ ergs}$, just allowing the small number of supernovae suggested by Rosado et al. (1996) from detailed modeling of the initial mass function. Note that the possible hidden SNR producing the excess X-ray emission would not yet have fully transferred its energy to the shell and so would currently make only a small contribution to the quoted input energy. The kinetic energy of the shell, from equation (5), is $K = (1\text{--}2) \times 10^{50}\text{ ergs}$. This model is definitely inconsistent with the dozens of supernovae suggested by Meaburn et al. (1989) based on the overall SN rate in the LMC and the size of the shell.

The age of the bubble is more problematic. From equation (3) and the above estimates of radius and expansion velocity, we find ages of $0.5\text{--}0.8\text{ Myr}$, well below the age of the central OB association. Another way of looking at it is that this bubble is expanding much too fast to have been produced by such an old OB association. Oey (1996) has demonstrated that this same phenomenon occurs in a number of superbubbles where the age of the central OB association has been measured. A possible solution to this problem may be that the expansion of the superbubble in a relatively low-density medium only occurs after it has

broken out of its parent molecular cloud, well after the formation of the central OB association. The association LH 10 in the nebula N11B, which we discuss next, may in fact be an example of just such an association that has formed but has not yet broken out into the low-density medium and produced a clear supershell. This suggestion supposes that the boundary between dense molecular cloud and diffuse ISM is significantly steeper than the r^{-2} power law that Oey (1996) examined. Further modeling of the process of superbubble breakout from molecular clouds appears useful.

5.2. N11B

An unconstrained spectral fit to this region gives a range in column density of $\log N_H = 20.0\text{--}22.0$ and temperature of $kT = 1.0\text{--}0.1$ keV. Constraining the absorbing column density independently, we find more reasonable values of $\log N_H = 21.3\text{--}21.6$ and $kT = 0.5\text{--}0.3$ keV. This corresponds to an X-ray luminosity $L_x = (0.3\text{--}0.9) \times 10^{35}$ ergs s^{-1} .

In order to estimate the X-ray emission contributed by OB stars in the central cluster LH 9, we first convert V -band fluxes of the 24 O and B stars located in a 4 arcmin² region centered on HD 32228 into bolometric magnitude (M_{bol}) by applying reddening (Parker et al. 1992) and bolometric (Chlebowski & Garmany 1991) corrections. We then convert the summed L_{bol} to X-ray luminosity by the relation $L_x = (1.4 \pm 0.3) \times 10^{-7} L_{bol}$, which is good for stars of types between O3 and A5 (Pallavicini et al. 1981; Chlebowski, Harnden, & Sciortino 1989). The overall stellar X-ray luminosity L_x is 5×10^{33} ergs s^{-1} , which is 6%–17% of the observed X-ray luminosity in N11B.

Figures 4b and 4c show two echellograms of the N11B region. The two slit positions are in a cross roughly centered on N11B, as shown in Figure 1b and described in § 2.3. They show well-resolved, remarkably Gaussian line profiles, with FWHM of 30–40 km s^{-1} . This FWHM includes an instrumental profile of 16 km s^{-1} and a thermal FWHM of 21 km s^{-1} . Taking half of the remaining width to be the typical motion of the gas, we find motions of 7–15 km s^{-1} , just supersonic, but not completely atypical for H II regions without shell structures. Figure 8 shows an example of one of these profiles at one of the few places where a high-velocity shoulder might be visible on the line. Other than

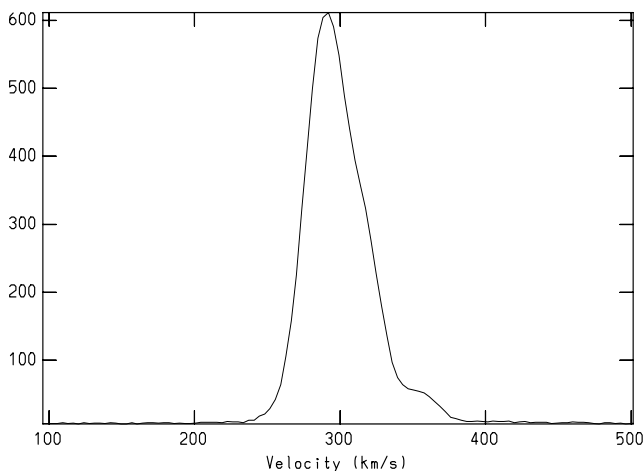


FIG. 8.—Velocity profile at the place designated by the thin black lines in Fig. 4c.

this shoulder, the lines appear quite featureless and completely lack high-velocity emission at velocities greater than 100 km s^{-1} .

The Carina Nebula resembles N11B in stellar content: both contain several O3 stars. A major difference between them is that the Carina Nebula shows an expanding shell structure in velocity and shows high-velocity gas at velocity offsets of several hundred km s^{-1} (Walborn 1982; Walborn & Hesser 1982), while N11B appears to have neither of these two dynamic features. The heating mechanism for the X-ray-emitting gas in Carina could be either stellar winds or SNRs.

The lack of a visible ring structure in N11B suggests that it contains no large cavity of hot gas. This makes it difficult to hide an SNR in the region. A supernova going off in a region with density greater than 0.1 cm⁻³ will generate classical SNR signatures (Tomisaka, Habe, & Ikeuchi 1981). We can find a lower bound to the density in N11B by assuming that it is a uniform, ionized sphere. The emission measure in H α is $\sim 4 \times 10^4$ cm⁻⁶ pc, and the diameter of the region is 27 pc, yielding an electron density of $n_e = 38$ cm⁻³. An SNR expanding into gas this dense would produce fireworks, in the form of the classical SNR signatures, none of which are observed. LH 10 contains between three and six O3 stars (Parker et al. 1992), suggesting that the cluster is extremely young, and adding further weight to the suggestion that no SNR has occurred yet.

If stellar winds do produce the observed X-ray emission, however, the question arises of why no clear stellar wind bubbles can be seen in N11B. A pressure-driven bubble would have a radius of (Weaver et al. 1977)

$$R = (28 \text{ pc})(\dot{M}_6 v_{2000}^2 n_0^{-1} t_6^3)^{1/5}, \quad (6)$$

where \dot{M}_6 is the mass-loss rate of the stellar wind in units of $10^{-6} M_\odot \text{ yr}^{-1}$, v_{2000} is the stellar wind velocity in units of 2000 km s^{-1} , and t_6 is the age of the bubble in units of 10^6 yr. Substituting a density of $n_0 = 38 \text{ cm}^{-3}$ and setting the other values to unity gives a bubble of radius 14 pc, or nearly an arcminute at the distance of the LMC. Indeed, Rosado et al. (1996) suggest a structure of overlapping bubbles based on their Fabry-Perot observations of the region in H α and [O III]. They found moderately broad H α lines, consistent with our echelle observations, as might be expected from many overlapping bubbles, and found that the narrower [O III] lines showed splitting indicative of small bubbles in some regions. Our H α image also shows some structure suggestive of overlapping bubbles; this can be seen even more clearly in the H α image of N11B shown in Walborn & Parker (1992). We have been awarded time to perform high-resolution imaging with the *Hubble Space Telescope* that may resolve this structure more clearly. *AXAF* imaging may reveal whether X-ray emission is confined to the interiors of such small wind-blown bubbles.

5.3. Other Shells

Shell 2 lies on the north edge of N11B. In H α emission, the shell appears elongated in the N-S direction, with a diameter of approximately 5' in that direction. However, the combination of the X-ray image and echelle spectroscopy by Meaburn et al. (1989) shows a different picture. X-rays are emitted only in the southern third of the bubble (see Fig. 3). Spectral fits with constrained absorption give a kT range of 0.3–0.4 keV and an X-ray luminosity of $(0.95\text{--}1.1) \times 10^{35}$ ergs s^{-1} in the 0.5–2.4 keV band. This region also turns out

to show a line splitting of $\sim 20 \text{ km s}^{-1}$ in the echelle spectrum. The region without X-ray emission also shows no line splitting in $\text{H}\alpha$. Thus, the X-ray emission is associated with a kinematically distinct structure of unknown origin.

Shell 3 lies adjacent to shell 2, north of the main bubble and NW of N11B. A kT range of 0.28–0.29 keV and an X-ray luminosity range of $(0.7\text{--}0.9) \times 10^{35} \text{ ergs s}^{-1}$ are derived from the constrained N_{H} fits. There is no clear boundary between the X-ray emission in the southern region of shell 2 and that of shell 3, although the $\text{H}\alpha$ morphology suggests that they are separate structures. The X-ray emission from shell 3 actually extends further to the west, possibly even merging with the plume of emission north of the SNR N11L. Spectroscopy of the region would be needed to further understand the relation among these structures.

Shell 4 lies south of the main bubble. Even the unconstrained fit shown in Figure 6 is quite close to the independently derived constraints on N_{H} . Spectral fits with constrained absorption give a kT range of 0.25–0.27 keV and an X-ray luminosity range of $(1.0\text{--}1.2) \times 10^{35} \text{ ergs s}^{-1}$. It is perhaps most remarkable in that it appears quite similar in $\text{H}\alpha$ morphology to the shell immediately to its east and yet has detectable X-ray emission, while the other shell does not. In the absence of any kinematical information from spectroscopy, we can only suggest that intermittent events such as hidden supernovae might produce such a pattern.

5.4. HD 32228

X-ray emission is observed in the PSPC map peaking at the position of the bright cluster HD 32228 (R.A. $04^{\text{h}}56^{\text{m}}34^{\text{s}}.5$; decl. $-66^{\circ}28'25''$; J2000) in the center of the main N11 shell (marked in Fig. 1a). However, no X-ray emission is seen in the HRI observation over 3σ or $2.3 \times 10^{-4} \text{ counts s}^{-1}$. This indicates that the X-ray luminosity from any point source associated with HD 32228 is below an upper limit of $L_{\text{x}} \sim 4 \times 10^{33} \text{ ergs s}^{-1}$.

The observed PSPC count rate within the 4 arcmin^2 region is $9.50 \times 10^{-4} \text{ counts s}^{-1}$. If we take the absorbing column density and local plasma temperature to be roughly the same as elsewhere in shell 1 ($kT \sim 3 \times 10^6 \text{ K}$, and $\log N_{\text{H}} \sim 21.0$, from Table 1), the observed X-ray luminosity is $L_{\text{x}} = 6.7 \times 10^{33} \text{ ergs s}^{-1}$. Following the same procedure used in § 5.2, we estimate the stellar X-ray luminosity to be $L_{\text{*}} \simeq (1.0 \pm 0.5) \times 10^{33} \text{ ergs s}^{-1}$. Therefore, the stellar X-ray emission accounts for only $\sim 15\%$ of the observed L_{x} , and the remaining emission is from the hot gas. HD 32228 does not appear to contain a compact object similar to those observed near R136 and R140 in 30 Dor (Wang 1995), showing that such X-ray sources are not universally associated with tight clusters such as this.

5.5. NW Region

The $\text{H}\alpha$ image shows faint filaments extending above shell 2 to the NW, in the box labeled “NW diffuse” in Figure 3. In this region there is an unidentified X-ray point source, as well as some diffuse X-ray emission that may be associated with the $\text{H}\alpha$ -emitting filaments. The spectrum of the point source suggests it is a Galactic foreground star. Its point nature has also been verified by its spatial profile in the HRI image. Therefore, X-ray emission from the point source is subtracted from the total PSPC flux. Spectral fits to the remaining emission with constrained absorption give

a kT of 0.3 keV in this region and an X-ray luminosity range of $(0.5\text{--}0.6) \times 10^{35} \text{ ergs s}^{-1}$. Similar diffuse X-ray emission has been observed outside the major structures visible in $\text{H}\alpha$ in N44 (Paper II) and 30 Dor (Chu 1996).

5.6. N11C

The X-ray emission in this region is dominated by a weak, pointlike source. Because of its small number of counts, the spectral fits do not confine well the plasma temperature and the absorption column density. We cannot confirm the point nature of this source, as it has luminosity below the detection limit of our HRI observation. The origin of this source is unclear.

6. CONCLUSIONS

1. The main bubble of N11, as defined from the $\text{H}\alpha$ morphology, surrounds the OB association LH 9. This shell outlines a region of bright X-ray emission with a luminosity of $(3\text{--}4) \times 10^{35} \text{ ergs s}^{-1}$, a factor of 3–7 times higher than the value predicted by an energy-conserving, pressure-driven superbubble model. This could be the result of an SNR hitting the inner edge of the shell (Paper I) or of a mass-loaded SNR in the interior (Arthur & Henney 1996). Both of these processes should produce intermittent and time-dependent excesses of X-ray emission over the prediction of the pressure-driven model. Indeed, the X-ray emission from the main bubble of N11 is only slightly above the predicted value, and the bubbles of Paper III all have upper limits on their luminosities consistent with the prediction. It remains true that no superbubble has yet been positively detected emitting with luminosity within a factor of 3 of the prediction of the pressure-driven model, although the limits are narrowing.

2. Diffuse X-ray emission is detected from N11B, a region analogous to the Carina Nebula with multiple O3 and other massive stars. The luminosity greatly exceeds that expected from the stars themselves, as in Carina. Unlike shell 1, the $\text{H}\alpha$ and X-ray morphology of N11B does not clearly suggest a shell, but rather a central condensation. Yet, echelle observations show supersonic motions, $\text{H}\alpha$ images show hints of overlapping shell structures, and the Fabry-Perot observations of $[\text{O III}]$ by Rosado et al. (1996) show line splitting in some regions. No gas moving at velocities over 60 km s^{-1} is seen, however, suggesting a lack of SNRs. Thus, we conclude that the diffuse X-ray emission could be powered solely by stellar winds from the central massive stars of LH 10.

The application to Carina is, unfortunately, less than incisive. An absence of emission from N11B in excess of stellar emission would have been strong support for the suggestion that hidden SNRs produce the X-ray emission in Carina, because the clusters are otherwise similar. However, the presence of bright X-ray emission from N11B does not argue against hidden SNRs in Carina, because of the presence of high-velocity gas in Carina and the absence of such gas in N11B.

3. The dynamical age of the main shell of N11 is under 1 Myr, significantly shorter than the age derived by Parker et al. (1992) for the central cluster, LH 9. This same problem has been found for other superbubbles by Oey (1996). We propose that the solution to this problem is that during the initial evolution of OB associations, they remain cocooned within their high-density parent molecular clouds and do not begin generating the observed superbubbles until after

they have broken out of the dense clouds into the surrounding diffuse ISM. N11B may be an example of a young OB association with energetic winds that has not yet broken out of a high-density region, since despite the presence of O3 stars and X-ray emission, very little high-velocity gas is observed, while CO is still observed toward this region.

4. The tight cluster HD 32228 in LH 9 is not a strong X-ray source, despite its resemblance in stellar density and size to the clusters R136 and R140 in 30 Dor. This suggests that the strong X-ray emission observed from R136 and R140 is not an intrinsic property of tight stellar clusters but is, rather, generated by a compact object that has formed there, as suggested by Wang (1995).

5. Three other shells seen in H α are associated with X-ray emission in the N11 region, with an integrated lumi-

nosity of $\sim 1 \times 10^{35}$ ergs s $^{-1}$. We named these structures shells 2, 3, and 4. In each case the association between the X-ray emission and the H α morphology is not as clear-cut as for shell 1 but still seems likely. Possibly the X-ray emission is a result of old or hidden supernovae. To understand the nature of these shells and the origin of the X-ray emission, more observations of the kinematics of the H α are required.

We thank G. García-Segura for participation in early stages of this project. S. D. P. acknowledges the hospitality of the Max-Planck-Institut für Astronomie and support from a National Science Foundation Graduate Fellowship. This research was partially supported by NASA grants NAG 5-2245 and NAG 5-1900.

REFERENCES

- Arthur, S. J., & Henney, W. J. 1996, *ApJ*, 457, 752
 Bloemen, H. 1989, *ARA&A*, 27, 469
 Bohlin, R. C., Savage, B. D., & Drake, J. F. 1978, *ApJ*, 224, 132
 Brunet, J. P. 1975, *A&A*, 43, 345
 Caldwell, D. A. 1996, *BAAS*, 28, 953
 Caldwell, D. A., & Kutner, M. L. 1996, *ApJ*, 472, 611
 Chlebowski, T., & Garmany, C. D. 1991, *ApJ*, 368, 241
 Chlebowski, T., Harnden, F. R., & Sciortino, S. 1989, *ApJ*, 341, 427
 Chu, Y.-H. 1996, in *Röntgenstrahlung from the Universe*, ed. H. U. Zimmermann, J. E. Trümper, & H. Yorke (Garching: Max-Planck-Institut für Extraterrestrische Physik), 311
 Chu, Y.-H., Chang, H., Su, Y., & Mac Low, M.-M. 1995, *ApJ*, 450, 157 (Paper III)
 Chu, Y.-H., & Mac Low, M.-M. 1990, *ApJ*, 365, 510 (Paper I)
 Chu, Y.-H., Mac Low, M.-M., García-Segura, G., Wakker, B., & Kennicutt, R. C. 1993, *ApJ*, 414, 213 (Paper II)
 Chu, Y.-H., Wakker, B. P., Mac Low, M.-M., & García-Segura, G. 1994, *AJ*, 108, 1696
 Cleary, M. N., Heiles, C., & Haslam, C. G. T. 1979, *A&AS*, 36, 95
 Cohen, R. S., Dame, T. M., Montani, J., Rubio, M., & Thaddeus, P. 1988, *ApJ*, 331, L95
 Conti, P. S., & Underhill, A. B. 1988, in *O Stars and Wolf-Rayet Stars* (NASA SP-497) (Washington: GPO)
 Corcoran, M. F., Swank, J., Rawley, G., Petre, R., Schmitt, J., & Day, C. 1994, in *The Soft X-Ray Cosmos*, ed. E. M. Schlegel & R. Petre (New York: AIP), 159
 Fitzpatrick, E. L. 1986, *AJ*, 92, 1068
 Fitzpatrick, E. L., & Savage, B. D. 1983, *ApJ*, 267, 93
 Henize, K. G. 1956, *ApJS*, 2, 315
 Israel, F. P., & de Graauw, Th. 1991, in *IAU Symp. 148, The Magellanic Clouds*, ed. R. Haynes & D. Milne (Dordrecht: Kluwer), 45
 Israel, F. P., et al. 1993, *A&A*, 276, 25
 Jenkins, E. B., Silk, J., & Wallerstein, G. 1976, *ApJS*, 32, 681
 Kennicutt, R. C., Jr., & Hodge, P. W. 1986, *ApJ*, 306, 130
 Lucke, P. B., & Hodge, P. W. 1970, *AJ*, 75, 171
 Mac Low, M.-M., & McCray, R. 1988, *ApJ*, 324, 776
 Meaburn, J., Solomos, N., Laspias, V., & Goudis, C. 1989, *A&A*, 225, 497
 Morrison, R., & McCammon, D. 1983, *ApJ*, 270, 119
 Oestreicher, M. O., Gochermann, J., & Schmidt-Kaler, T. 1995, *A&AS*, 112, 495
 Oestreicher, M. O., & Schmidt-Kaler, T. 1996, *A&AS*, 117, 303
 Oey, M. S. 1996, *ApJ*, 467, 666
 Pallavicini, R., Golub, L., Rosner, R., Vaiana, G. S., Ayres, T., & Linsky, J. L. 1981, *ApJ*, 248, 279
 Panagia, N., Gilmozzi, R., Macchetto, F., Adorf, H.-M., & Kirshner, R. P. 1991, *ApJ*, 380, L23
 Parker, J. Wm., Garmany, C. D., Massey, P., & Walborn, N. R. 1992, *AJ*, 103, 1205
 Parker, J. Wm., Hill, J. K., Bohlin, R. C., O'Connell, R. W., Neff, S. G., Roberts, M. S., Smith, A. M., & Stecher, T. P. 1996, *ApJ*, 472, L29
 Pfeffermann, E., et al. 1986, *SPIE*, 733, 519
 Raymond, J. C., & Smith, B. W. 1977, *ApJS*, 35, 419
 Rohlfs, K., Kreitschmann, J., Siegmán, B. C., & Feitzinger, J. V. 1984, *A&A*, 137, 343
 Rosado, M., Laval, A., Le Coarer, E., Georgelin, Y. P., Amram, P., Marcelin, M., Goldes, G., & Gach, J. L. 1996, *A&A*, 308, 588
 ROSAT Mission Description. 1991, NASA NRA 91-OSSA-3, Appendix F
 Schwoering, P. B. W., & Israel, F. P. 1991, *A&A*, 246, 231
 Seward, F. D., & Chlebowski, T. 1982, *ApJ*, 256, 530
 Snowden, S. L., & Petre, R. 1994, *ApJ*, 436, L123
 Tao, L. 1995, *MNRAS*, 275, 965
 Tomisaka, K., Habe, A., & Ikeuchi, S. 1981, *Ap&SS*, 78, 273
 Walborn, N. R. 1982, *ApJS*, 48, 145
 Walborn, N. R., & Hesser, J. 1982, *ApJ*, 252, 156
 Walborn, N. R., & Parker, J. Wm. 1992, *ApJ*, 399, L87
 Wang, Q. D. 1995, *ApJ*, 453, 783
 Wang, Q., & Helfand, D. J. 1991a, *ApJ*, 370, 541
 ———. 1991b, *ApJ*, 373, 497
 Weaver, R., McCray, R., Castor, J., Shapiro, P., & Moore, R. 1977, *ApJ*, 208, 610